

ORIGINAL ARTICLE

Open Access



Effects of Four Types of Pre-swirls on the Leakage, Flow Field, and Fluid-Induced Force of the Rotary Straight-through Labyrinth Gas Seal

Qingfeng Wang^{1,2*} and Lidong He^{1,2}

Abstract

The labyrinth seal in turbomachinery is a key element that restricts leakage flow among rotor-stator clearances from high-pressure regions to low-pressure regions. The fluid-induced forces on the rotor from seals during machine operation must be accurately quantified to predict their dynamic behavior effectively. To understand the fluid-induced force characteristics of the labyrinth seal more fully, the effects of four types of pre-swirls on the leakage, flow field, and fluid-induced force of a rotary straight-through labyrinth gas seal (RSTLGS) were numerically investigated using the proposed steady computational fluid dynamics (CFD) method based on the three-dimensional models of the RSTLGS. The leakage, flow field, and fluid-induced force of the RSTLGS for six axial pre-swirl velocities, four radial pre-swirl angles, four circumferential positive pre-swirl angles, and four circumferential negative pre-swirl angles were computed under the same geometrical parameters and operational conditions. Mesh analysis ensures the accuracy of the present steady CFD method. The numerical results show that the four types of pre-swirls influence the leakage, flow field, and fluid-induced force of the RSTLGS. The axial pre-swirl velocity remarkably inhibits the fluid-induced force, and the circumferential positive pre-swirl angle and circumferential negative pre-swirl angle remarkably promote the fluid-induced force. The effects of the radial pre-swirl angle on the fluid-induced force are complicated, and the pressure forces and viscous forces show the maximum or minimum values at a specific radial pre-swirl angle. The pre-swirl has a negligible impact on the leakage. The four types of pre-swirls affect the leakage, flow field, and fluid-induced force of the RSTLGS to varying degrees. The pre-swirl is the influence factor affecting the leakage, flow field, and fluid-induced force of the RSTLGS. The conclusions will help to understand the fluid-induced force of labyrinth seals more fully, by providing helpful suggestions for engineering practices and a theoretical basis to analyze the fluid–structure interaction of the seal-rotor system in future research.

Keywords: Rotary straight-through labyrinth gas seal, Pre-swirl, Leakage, Flow field, Fluid-induced force

1 Introduction

Turbomachineries contain numerous labyrinth seals operating within close proximity to rotating parts, for preventing flow recirculation in the compressor and turbine stages, to meter cooling air to various parts of the

engine, and to ensure that the main flow does not enter into the rotor bearing cavities [1–3]. The major advantages of the labyrinth seal are simplicity, reliability, and tolerance to large thermal and pressure variations, and it is unlikely to be replaced in the future [4–6]. The fluid–structure interaction of the seal-rotor system can result in self-excited shaft vibrations of the turbomachinery; often the amplitude of the vibrations becomes unacceptably high and the scheduled power or running speed cannot be achieved [7]. One of the most important sources of excitation is the flow through the labyrinth seal, which

*Correspondence: 123188234@qq.com

¹ Beijing Key Laboratory of Health Monitoring and Self-Recovery for High-End Mechanical Equipment, Beijing University of Chemical Technology, Beijing 100029, China

Full list of author information is available at the end of the article

has been an engine development problem since the 1960s [8, 9], and the first comprehensive study in this regard was proposed by Alford [10]. Although the main function of the labyrinth seal is to control leakage, the fluid–structure interaction between the rotor and seal stator components directly affects rotor vibration and stability [11]. As these seal forces can stabilize or destabilize the rotor system and affect the vibration response of modern turbomachinery, they must be controlled to ensure that the rotor system of the turbomachinery remains stable throughout its operational duration [12]. In response to the constantly increasing demands for aggressive power output, efficiency, and operational life, turbomachinery is being designed to operate at higher temperature, higher pressure, and higher rotational speed [13]. Consequently, there is a need to study the fluid-induced force of the labyrinth seal.

To understand the flow characteristics of the labyrinth seal more fully, and to improve the design performance in labyrinth seals, three methods are mostly used in the available publications: experimental [14–16], mathematical computation [17–19], and numerical simulation [20–25]. Computational fluid dynamics (CFD) is an established industrial design tool that helps to reduce design time scales and improve processes throughout the engineering world. CFD provides a cost-effective and accurate alternative to scale model testing, where variations on the simulation are performed quickly, which offers evident advantages. With the CFD program, the numerical simulation method has been used to study the leakage flow and rotordynamic characteristics of labyrinth seals by Moore [20], Hirano et al. [21], Pugachev et al. [22], and Subramanian et al. [24].

Although many studies have been conducted to investigate the rotordynamic coefficients of the labyrinth seal, the fluid-induced force of the labyrinth seal is not fully understood. For example, the effects of the pre-swirl on the fluid-induced force and the corresponding disciplines must be further studied [26–28]. To obtain a more detailed insight into the fluid-induced force of the labyrinth seal, the present study applies the steady CFD method based on the three-dimensional model of the rotary straight-through labyrinth gas seal (RSTLGS). To investigate the effects of four types of pre-swirls, the leakage, flow field, and fluid-induced force of the RSTLGS are computed for six axial pre-swirl velocities, four radial pre-swirl angles, four circumferential positive pre-swirl angles, and four circumferential negative pre-swirl angles under the same geometrical parameters and operational conditions. The primary objective of this work is numerical investigation of the effects of the four

types of pre-swirls on the leakage, flow field, and fluid-induced force of the RSTLGS.

2 Governing Equations

CFD is a computer-based tool for simulating the behavior of systems involving fluid flow, heat transfer, and other related physical processes. It solves the equations of fluid flow over a region of interest, with specified conditions on the boundary of that region. The equations that describe the processes of momentum, heat, and mass transfer are known as the Navier–Stokes equations. Various solution methods are used in CFD codes. The most common method, and the one on which the software CFX is based, is known as the finite volume technique.

The equations of mass, momentum, and energy solved using ANSYS CFX are the unsteady Navier–Stokes equations in their conservation form. The Navier–Stokes equations describe both laminar and turbulent flows without the need for additional information. Turbulence consists of fluctuations in the flow field in time and space. It is a complex process, mainly because it is three-dimensional, unsteady, and consists of many scales. It can have a significant effect on the characteristics of the flow. Turbulence occurs when the inertial forces in the fluid become significant compared with viscous forces, and is characterized by a high Reynolds number.

To predict the effects of turbulence, numerous CFD studies have focused on the use of turbulence models. Turbulence models have been specifically developed to account for the effects of turbulence without recourse to a prohibitively fine mesh and direct numerical simulation. In general, turbulence models seek to modify the original unsteady Navier–Stokes equations by introducing averaged and fluctuating quantities to produce the Reynolds-averaged Navier–Stokes (RANS) equations. The RANS equations of mass, momentum, and energy conservation can be expressed as follows [29]:

The continuity equation:

$$\frac{\partial \rho}{\partial t} + \nabla \cdot (\rho U) = 0. \quad (1)$$

The momentum equations:

$$\frac{\partial(\rho U)}{\partial t} + \nabla \cdot (\rho U \otimes U) = \nabla \cdot \{ \tau - \rho \overline{u \otimes u} \} + \mathcal{S}_M. \quad (2)$$

The Reynolds-averaged energy equation:

$$\begin{aligned} \frac{\partial(\rho h_{tot})}{\partial t} - \frac{\partial p}{\partial t} + \nabla \cdot (\rho U h_{tot}) \\ = \nabla \cdot \left(\lambda \nabla \tau - \rho \overline{u h_{stat}} \right) + \nabla \cdot (U \cdot \tau) + \mathcal{S}_E. \end{aligned} \quad (3)$$

Here, τ is the molecular stress tensor, h_{tot} is the mean total enthalpy, S_M is the momentum source and S_E is the energy source. The term $\rho \overline{u \otimes u}$ indicates the Reynolds stresses and the term $\rho \overline{u h_{stat}}$ is the Reynolds flux. The term $\nabla \cdot (U \cdot \tau)$ represents the work owing to viscous stresses and is called the viscous work term.

Simulation of the RANS equations considerably reduces the computational effort compared with a direct numerical simulation, and is generally adopted for practical engineering calculations. The Reynolds stresses must be modeled using additional equations of known quantities to close the system according to the type of turbulence model. Turbulence models close the Reynolds-averaged equations by providing models for the computation of the Reynolds stresses and Reynolds fluxes. CFX models can be broadly divided into two classes: eddy viscosity models and Reynolds stress models. In this work, the shear stress transport (SST) model in ANSYS CFX 17.0 is chosen to simulate the fluid flow in the seal. The SST model accounts for the transport of the turbulent shear stress and provides highly accurate predictions of the onset and amount of flow separation under adverse pressure gradients.

3 Numerical Calculation Method

3.1 Numerical Computational Model

According to the conventional straight-through labyrinth seal, the geometry of the RSTLGS is shown in Figure 1. Table 1 provides the detailed geometrical parameters and operational conditions for the steady CFD analyses.

Figure 2 shows the computational model and mesh of the RSTLGS. As the geometry of the RSTLGS is non-axisymmetric and the circumferential fluid-induced forces in the whirling RSTLGS are nonuniform, a three-dimensional computational model with eccentricity is required to obtain the flow characteristics using the steady CFD. In this work, the commercial software ANSYS DesignModeler 17.0 and ANSYS ICEM CFD 17.0 are used to generate the three-dimensional computational model and unstructured mesh for the calculations, respectively.

3.2 Numerical Computational Parameters

In this work, the flow field and fluid-induced force were numerically predicted for the RSTLGS using the steady CFD method based on three-dimensional models. The present steady CFD analyses were conducted using the commercial software ANSYS-CFX 17.0 to solve the RANS equations. Table 2 lists the detailed numerical approaches and parameters used for the steady CFD analyses. The SST model was applied to model the turbulence characteristics of the flow. The high-resolution scheme was applied as the advection scheme and for turbulence

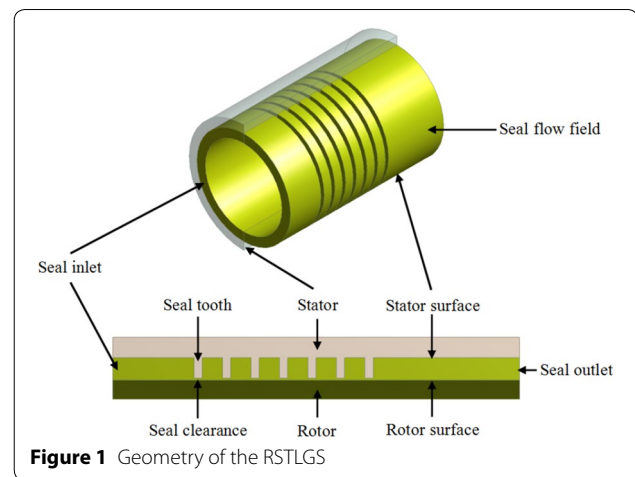


Figure 1 Geometry of the RSTLGS

numerics. Based on the past CFD analyses and computational convergence [20–25], the flow regime (subsonic), opening pressure (relative pressure), flow direction (normal to the boundary condition), and turbulence quantities (turbulence intensity = 5%) were defined for the seal inlet and outlet boundaries. The inlet pre-swirl velocity was considered negligible.

To obtain the flow field and fluid-induced force of the RSTLGS, the calculation with a whirling rotor is necessary, where the rotor whirls and spins around the center of the seal stator and rotor, respectively. In a stationary frame of reference, the geometry of the rotor appears to be moving, and hence, the moving grid and transient analyses are necessary. However, in a rotating frame of reference, the rotor remains fixed, and the analysis becomes steady-state. Hence, the rotating reference frame with ω is selected in this work. In the rotating reference frame, it is assumed that the speeds of the seal rotor and seal fluid are ω , the axis of the rotating reference frame is the axis of the seal rotor, and the seal fluid is eccentric.

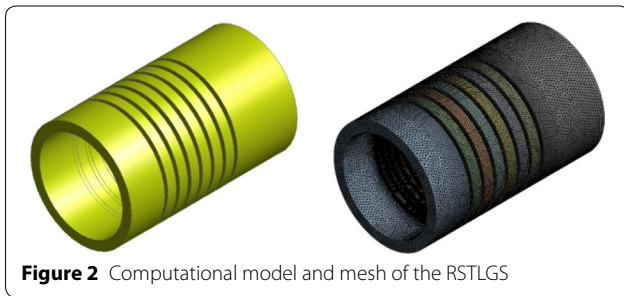
3.3 Computational Mesh Analysis

To determine the necessary mesh density for predicting the flow characteristics of the RSTLGS accurately, a mesh analysis was performed. The geometrical parameters and boundary conditions are shown in Tables 1 and 3, respectively. In the analysis, the inlet pressure and outlet pressure were 1000000 and 0 Pa, respectively. A total of 12 cases were selected and computed for 3 types of relevance centers (fine, medium, coarse) and 4 types of relevance (25, 50, 75, 100), as shown in Table 4.

According to the accuracy and speed of the calculations, the mesh in case 6 was selected for subsequent computations of the RSTLGS. In case 6, there were

Table 1 Geometrical dimensions and operation conditions

Parameter	Value
Seal length (m)	0.1
Seal inlet length (m)	0.02
Seal clearance (m)	0.0005
Seal tooth height (m)	0.005
Seal tooth width (m)	0.002
Seal tooth pitch (m)	0.005
Rotor diameter (m)	0.05
Tooth number	7
Eccentricity (m)	0.0002
Rotational speed ω (rad/s)	500
Inlet pressure (Pa)	50000
Outlet pressure (Pa)	0

**Figure 2** Computational model and mesh of the RSTLGS**Table 2 Numerical computational parameters**

Parameter	Value
Solution type	Steady
Fluid	Air at 25 °C
Computational method	Time marching method
Turbulence model	Shear stress transport
Wall properties	Adiabatic, smooth surface
Advection scheme	High resolution
Turbulence numerics	High resolution
Minimum number of iterations	1
Maximum number of iterations	400
Residual type	RMS
Residual target	0.0001

2.5589×10^6 elements and 5.8281×10^5 nodes; the sizes of the minimum element, maximum face element, and maximum tetrahedron element were 2.2757×10^{-5} m, 2.2757×10^{-3} m, and 4.5515×10^{-3} m, respectively.

4 Analysis Method

In this work, the leakage, flow field, and fluid-induced force of the RSTLGS are analyzed in terms of the leakage flow rates, velocity vectors, velocity streamlines,

Table 3 Boundary conditions

Parameter	Value
Inlet	Total pressure (stable)
Outlet	Opening pressure and direction
Seal wall	No slip wall
Rotor wall	Angular velocity 500 rad/s

total pressure distributions on the rotor surface, pressure forces, and viscous forces. The pressure force and viscous force are affected by the seal flow field on the rotor surface. The pressure force results from the pressures on the rotor surface. In this study, the pressure forces on the rotor surface are composed of the radial pressure force, axial pressure force, and total pressure force. The radial pressure force results from the pressure components in the X and Y directions; the axial pressure force results from the pressure component in the Z direction; the total pressure force is the sum of the pressure components in the X , Y , and Z directions, all of which are numerically calculated. The viscous force results from the shear forces on the rotor surface. In this study, the viscous forces on the rotor surface are composed of the radial viscous force, axial viscous force, and total viscous force. The radial viscous force includes the viscous force components in the X and Y directions; the axial viscous force is the viscous force component in the Z direction; the total viscous force results from the viscous force components in the X , Y , and Z directions, all of which are numerically calculated.

To investigate the effects of four types of pre-swirls on the leakage, flow field, and fluid-induced force of the RSTLGS, in this work, the computations were performed for six axial pre-swirl velocities, four radial pre-swirl angles, four circumferential positive pre-swirl angles, and four circumferential negative pre-swirl angles, as shown in Table 5.

Figure 3 illustrate the four types of pre-swirls. The axial pre-swirl signifies that the direction of the initial fluid entering a seal is perpendicular to the inlet cross-section. The radial pre-swirl signifies that the direction of the initial fluid entering a seal is along the radial direction of the seal and is oblique to the inlet cross-section. The circumferential pre-swirl signifies that the direction of the initial fluid entering a seal is along the circumferential direction of the seal and is oblique to the inlet cross-section. The circumferential positive pre-swirl indicates the initial fluid swirl in a direction identical to the rotor rotation direction, and the circumferential negative pre-swirl indicates the initial fluid swirl in a direction opposite to the rotor rotation direction.

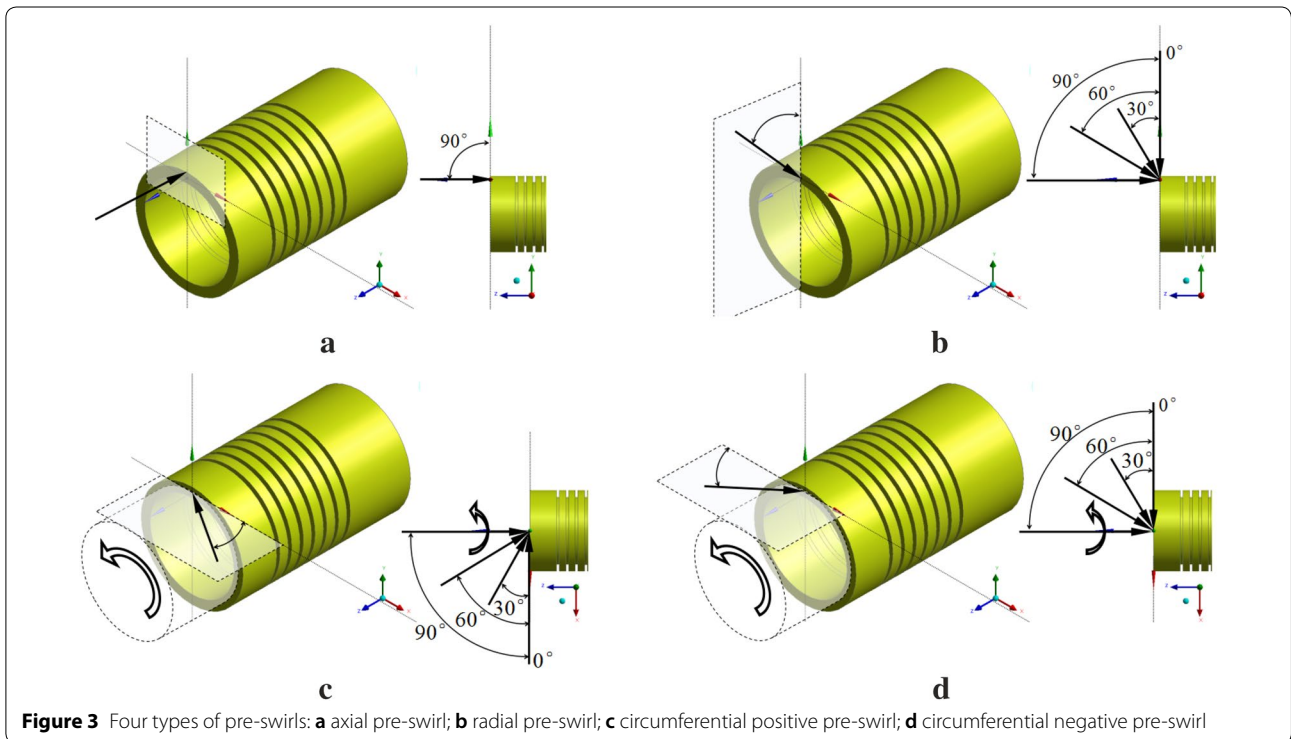
Table 4 Computational mesh comparison

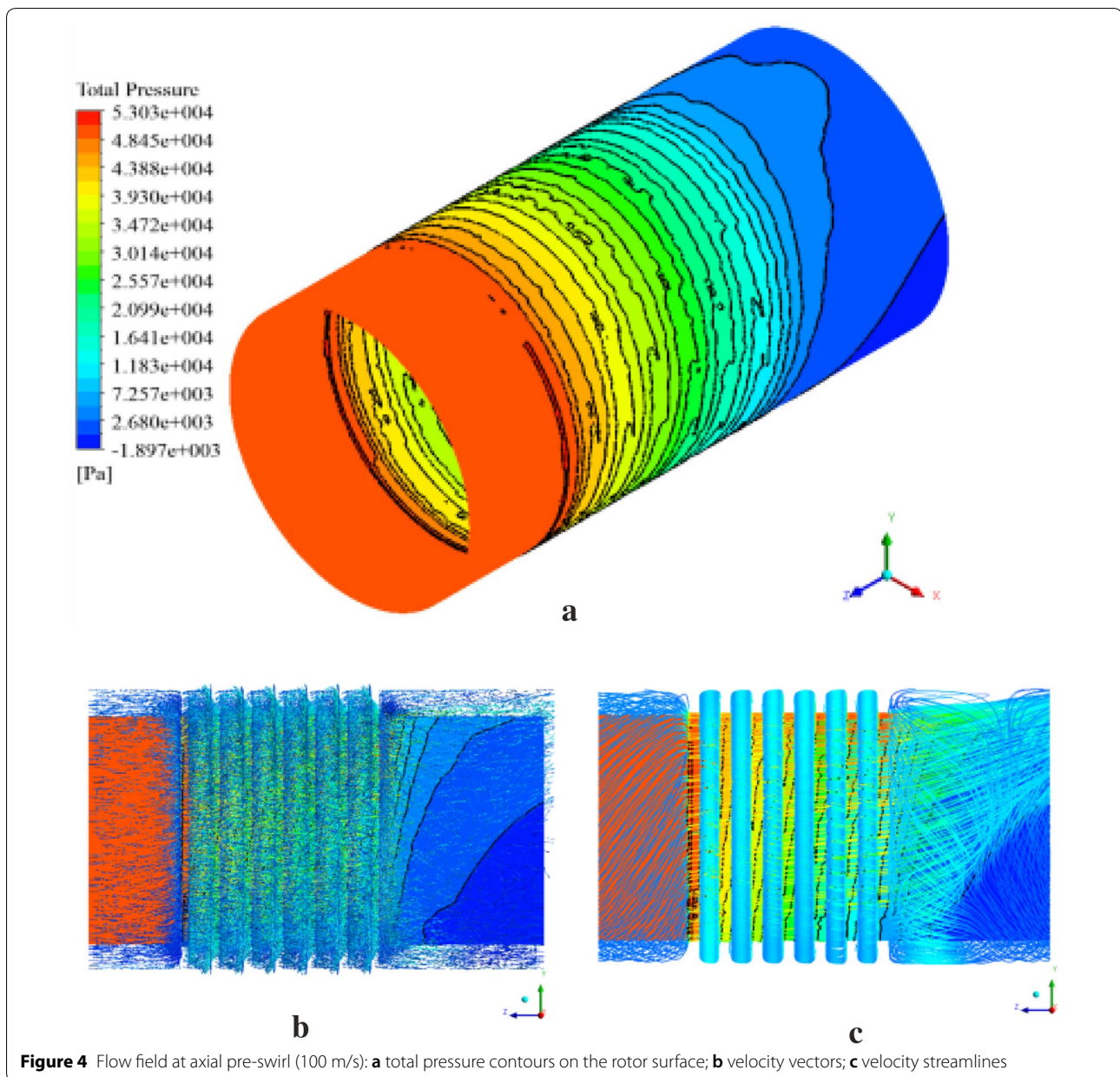
Case	Relevance center	Relevance	Elements	Nodes	Leakage (kg/s)	Computing time (s)
1	Fine	100	8115473	1826912	0.042067	5021
2	Fine	75	5251659	1259816	0.04106	3223
3	Fine	50	3720923	935495	0.040115	1927
4	Fine	25	2920397	746032	0.040115	1861
5	Medium	100	3926473	841153	0.040633	2698
6	Medium	75	2558894	582811	0.039475	1576
7	Medium	50	1787700	418855	0.038905	1011
8	Medium	25	1322674	314406	0.038594	756
9	Coarse	100	1235191	260690	0.037593	951
10	Coarse	75	807851	179545	0.036591	538
11	Coarse	50	550481	127732	0.035812	352
12	Coarse	25	415661	96077	0.035899	282

Table 5 Pre-swirl parameters

Pre-swirl	Velocity (m/s)	Angle (°)
Axial	0, 50, 100, 150, 200, 250	90
Radial	100	0, 30, 60, 90
Circumferential positive	100	0, 30, 60, 90
Circumferential negative	100	0, 30, 60, 90

Based on the computation results, the change rates of the leakage flow rates, pressure forces on the rotor surface, and viscous forces on the rotor surface were calculated to understand the effects of the four types of inlet pre-swirl better. The change rate, which is the variation-to-initial-value ratio of the leakage flow rates, pressure forces on the rotor surface, and viscous forces on the rotor surface,





reflects the effects of the four types of inlet pre-swirl on the leakage, flow field, and fluid-induced force.

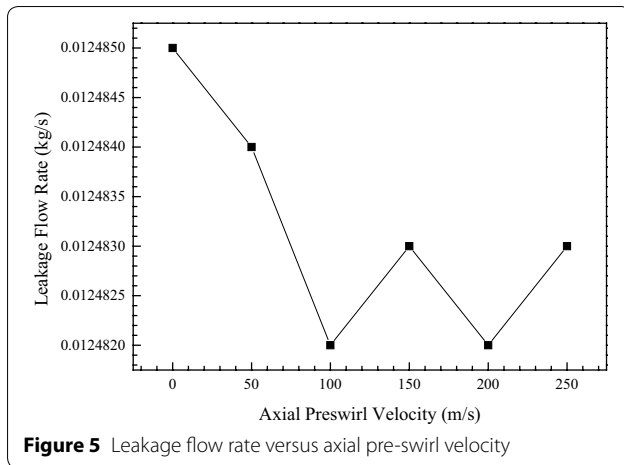
5 Results and Discussion

5.1 Flow Field

To investigate the effects of the pre-swirl on the flow field of the RSTLGS, the total pressure distributions on the rotor surface, velocity vectors, and velocity streamlines through the seal were computed.

Figure 4 shows the flow field at axial pre-swirl (100 m/s), and Figure 4(a)–(c), respectively, show the total pressure contours on the rotor surface, velocity vectors,

and velocity streamlines through the seal. As shown in Figure 4(a), the pressure drop from the seal inlet to the outlet is 50000 Pa, the seal inlets are high-pressure areas, the seal outlets are low-pressure areas, the total pressure of the seal cavities gradually decreases through the seal, and the total pressure contour distributions on the rotor surface gradually change from axisymmetric to non-axisymmetric through the seal. As shown in Figure 4(b) and (c), the velocity vectors and the velocity streamlines through the seal revolve around the rotor, those in the grooves of the seal have secondary circulation flow, and those in the outlet of the seal have eccentric circulation



vortex. The flow field of the RSTLGS with the eccentric flow rotates around the axis of the seal rotor and generates fluid-induced force.

5.2 Effects of the Axial Pre-swirl

To investigate the effects of the axial pre-swirl velocity on the fluid-induced force of the RSTLGS, the leakage flow rates, pressure forces, and viscous forces were computed for six axial pre-swirl velocities.

Figure 5 illustrates the dependence of the leakage flow rates for all six axial pre-swirl velocities. With increasing axial pre-swirl velocity, the leakage flow rate first decreases approximately 0.02% from 0.012485 kg/s at 0 m/s to 0.012482 kg/s at 100 m/s, and subsequently fluctuates from 0.012482 kg/s at 100 m/s to 0.012483 kg/s at 250 m/s. Therefore, the leakage flow rate decreases and then continues fluctuating with increasing axial pre-swirl velocity.

Figure 6 illustrates the dependence of the pressure forces on the rotor surface for all six axial pre-swirl velocities. With increasing axial pre-swirl velocity, the radial pressure force first increases approximately 1.61% from 0.735399 N at 0 m/s to 0.747210 N at 50 m/s, subsequently decreases approximately 3.31% from 0.747210 N at 50 m/s to 0.722497 N at 100 m/s, and then begins to stabilize from 0.722497 N at 100 m/s to 0.721998 N at 250 m/s; a peak at 50 m/s appears. With increasing axial pre-swirl velocity, the axial pressure force first decreases approximately 0.03% from 0.052541 N at 0 m/s to 0.052527 N at 100 m/s, subsequently increases approximately 0.002% from 0.052527 N at 100 m/s to 0.052528 N at 250 m/s, and then begins to stabilize from 0.052528 N at 200 m/s to 0.052528 N at 250 m/s; a valley at 100 m/s appears. With increasing axial pre-swirl velocity, the total pressure force first increases approximately 1.60% from 0.737273 N at 0 m/s to 0.749055 N

at 50 m/s, subsequently decreases approximately 3.29% from 0.749055 N at 50 m/s to 0.724404 N at 100 m/s, and then begins to stabilize from 0.724404 N at 100 m/s to 0.723906 N at 250 m/s; a peak at 50 m/s appears. Therefore, the radial and total pressure forces first increase, subsequently decrease, and then begin to stabilize with increasing axial pre-swirl velocity; the axial pressure force first decreases, and then begins to stabilize with increasing axial pre-swirl velocity. The radial pressure force is much larger than the axial pressure force, and hence, the radial pressure force is the main component of the total pressure force.

Figure 7 illustrates the dependence of the viscous forces on the rotor surface for all six axial pre-swirl velocities. With increasing axial pre-swirl velocity, the radial viscous force first increases approximately 1.25% from 0.012853 N at 0 m/s to 0.013014 N at 50 m/s and subsequently decreases approximately 0.81% from 0.013014 N at 50 m/s to 0.012908 N at 250 m/s; a peak at 50 m/s appears. With increasing axial pre-swirl velocity, the axial viscous force first decreases approximately 0.04% from 0.656590 N at 0 m/s to 0.656320 N at 100 m/s and subsequently increases approximately 0.009% from 0.656320 N at 100 m/s to 0.656380 N at 250 m/s; a valley at 100 m/s appears. With increasing axial pre-swirl velocity, the total viscous force first decreases approximately 0.04% from 0.656716 N at 0 m/s to 0.656448 N at 100 m/s and subsequently increases approximately 0.009% from 0.656448 N at 100 m/s to 0.656507 N at 250 m/s; a valley at 100 m/s appears. Therefore, the radial viscous force first increases and subsequently decreases with increasing axial pre-swirl velocity; the axial and total viscous forces first decrease and subsequently increase with increasing axial pre-swirl velocity. The radial viscous force is much smaller than the axial viscous force, and hence, the axial viscous force is the main component of the total viscous force.

5.3 Effects of the Radial Pre-swirl

To investigate the effects of the radial pre-swirl angle on the fluid-induced force of the RSTLGS, the leakage flow rates, pressure forces, and viscous forces were computed for four radial pre-swirl angles at a pre-swirl velocity (100 m/s).

Figure 8 illustrates the dependence of the leakage flow rates for all four radial pre-swirl angles. With increasing radial pre-swirl angle, the leakage flow rate first remains stable from 0.012484 kg/s at 0° to 0.012484 kg/s at 30°, subsequently decreases approximately 0.02% from 0.012484 kg/s at 30° to 0.012482 kg/s at 60°, and then remains stable from 0.012482 kg/s at 60° to 0.012482 kg/s at 90°. Therefore, the leakage flow rate decreases with increasing radial pre-swirl angle.

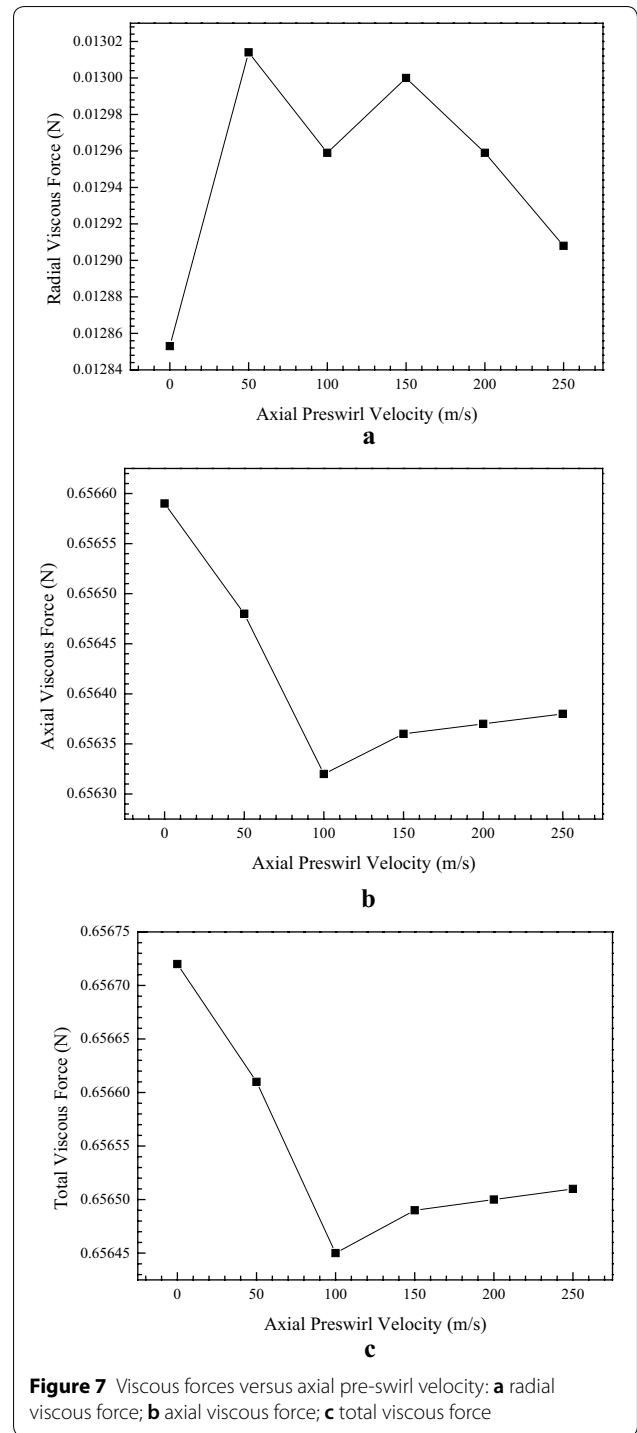
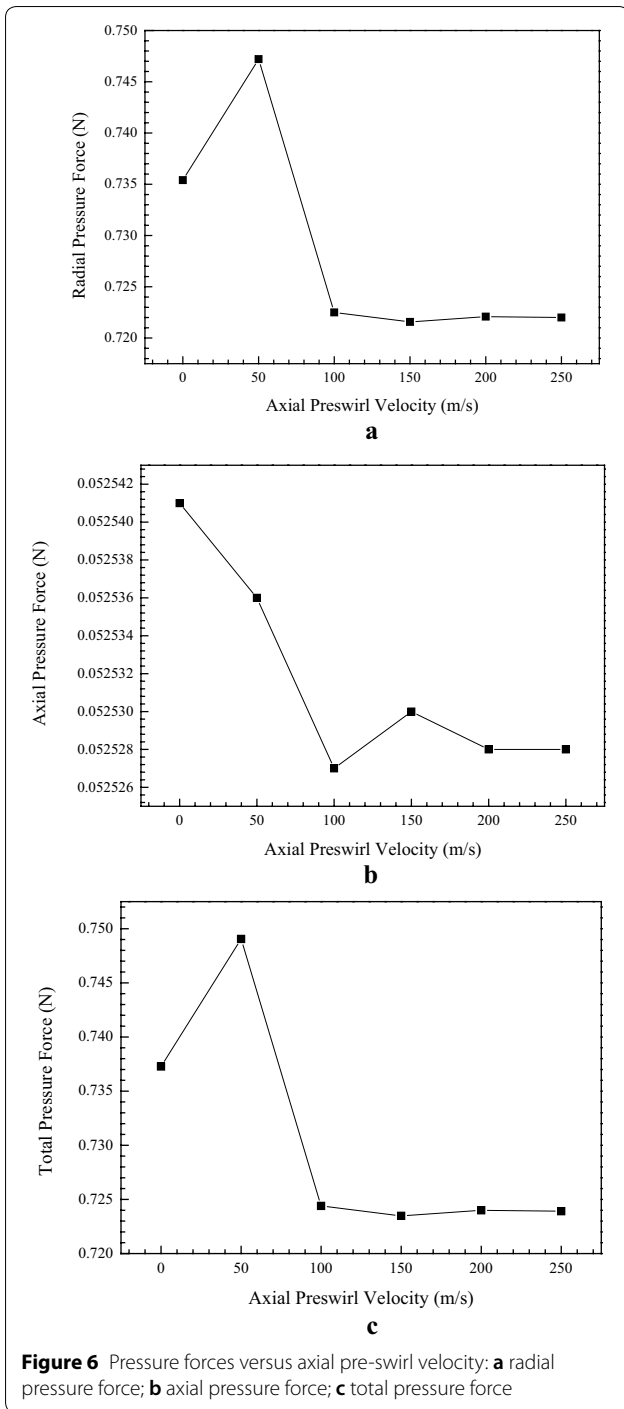
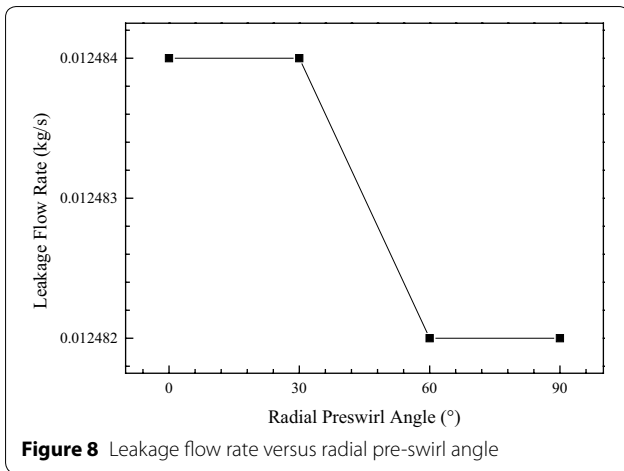


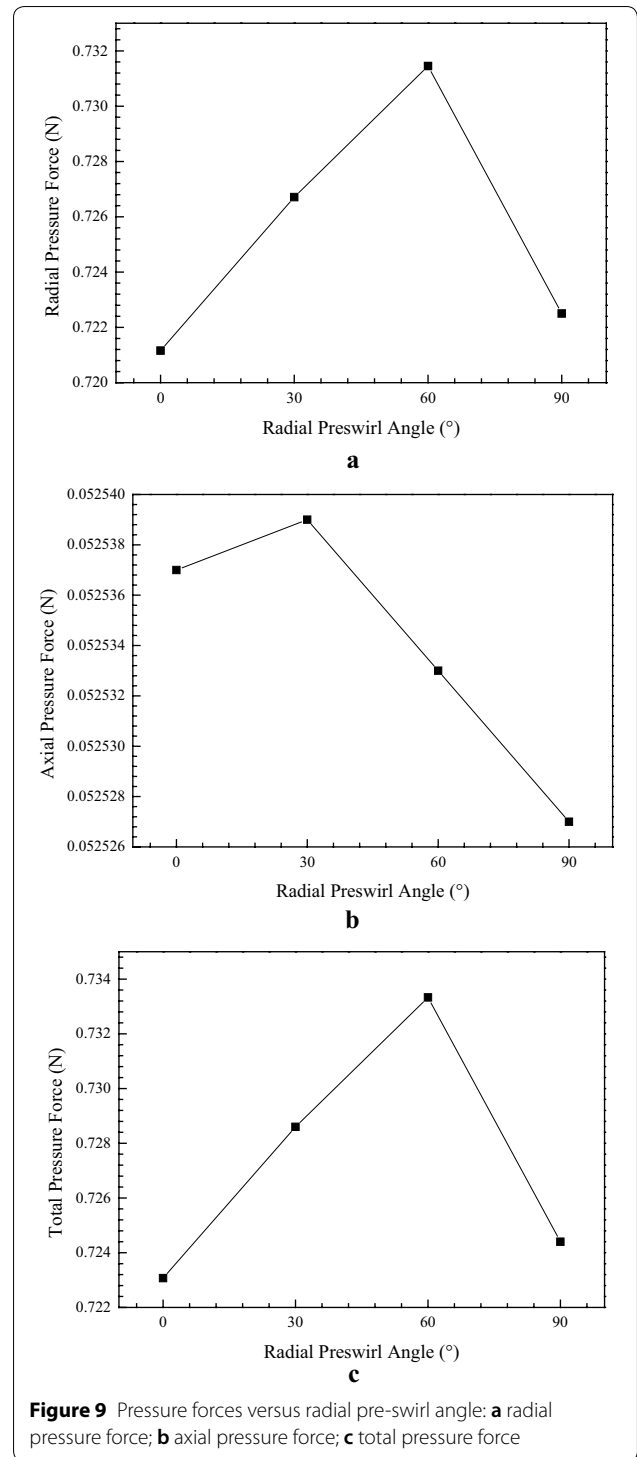
Figure 9 illustrates the dependence of the pressure forces on the rotor surface for all four radial pre-swirl angles. With increasing radial pre-swirl angle, the radial pressure force first increases by approximately 1.43% from 0.721157 N at 0° to 0.731446 N at 60°, and subsequently decreases by approximately 1.22% from

0.731446 N at 60° to 0.722497 N at 90°; a peak at 60° appears. With increasing radial pre-swirl angle, the axial pressure force first increases by approximately 0.004% from 0.052537 N at 0° to 0.052539 N at 30°, and subsequently decreases by approximately 0.02% from 0.052539 N at 30° to 0.052527 N at 90°; a peak at



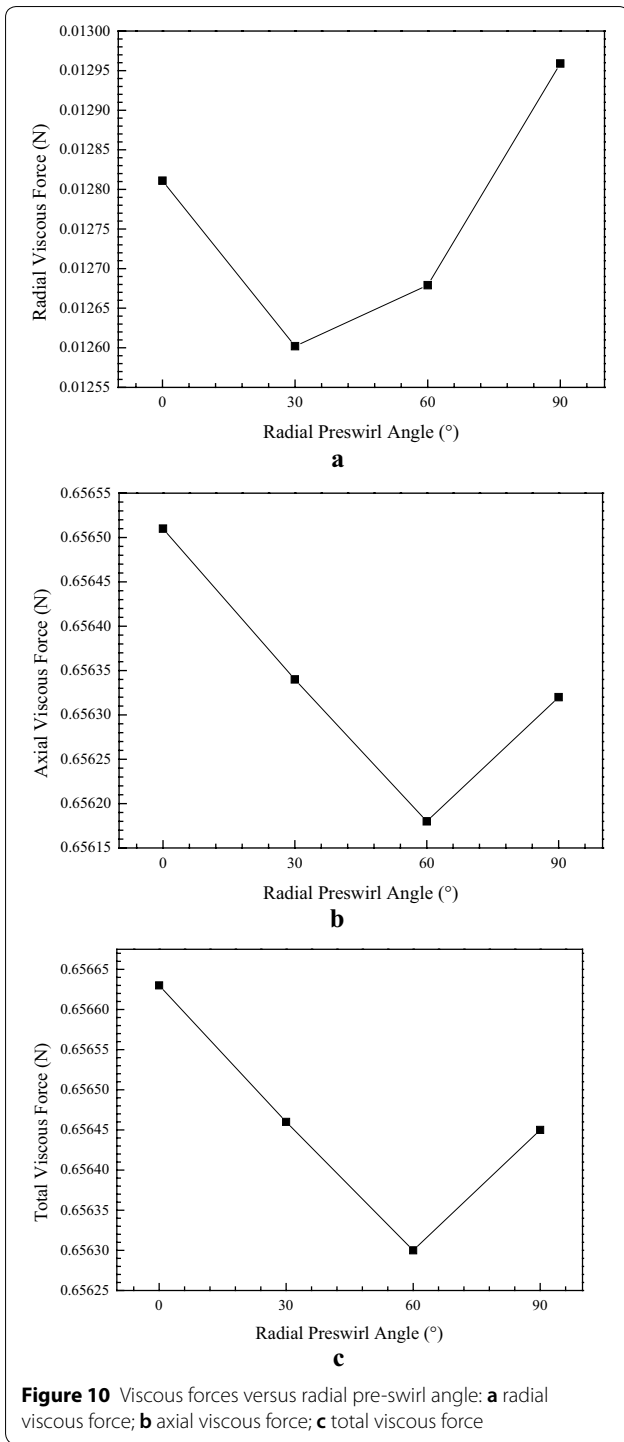
30° appears. With increasing radial pre-swirl angle, the total pressure force first increases by approximately 1.42% from 0.723068 N at 0° to 0.733330 N at 60°, and subsequently decreases by approximately 1.22% from 0.733330 N at 60° to 0.724404 N at 90°; a peak at 60° appears. Therefore, the radial, axial, and total pressure forces first increase and subsequently decrease with increasing radial pre-swirl angle, and the pressure forces show maximum values. The radial pressure force is much larger than the axial pressure force, and hence, the radial pressure force is the main component of the total pressure force.

Figure 10 illustrates the dependence of the viscous forces on the rotor surface for all four radial pre-swirl angles. With increasing radial pre-swirl angle, the radial viscous force first decreases by approximately 1.63% from 0.012811 N at 0° to 0.012602 N at 30°, and subsequently increases by approximately 2.83% from 0.012602 N at 30° to 0.012959 N at 90°; a valley at 30° appears. With increasing radial pre-swirl angle, the axial viscous force first decreases by approximately 0.05% from 0.656510 N at 0° to 0.656180 N at 60°, and subsequently increases by approximately 0.02% from 0.656180 N at 60° to 0.656320 N at 90°; a valley at 30° appears. With increasing radial pre-swirl angle, the total viscous force first decreases by approximately 0.05% from 0.656635 N at 0° to 0.656302 N at 60°, and subsequently increases by approximately 0.02% from 0.656302 N at 60° to 0.656448 N at 90°; a valley at 60° appears. Therefore, the radial, axial, and total viscous forces first decrease and subsequently increase with increasing radial pre-swirl angle, and the viscous forces show minimum values. The radial viscous force is less than the axial viscous force, and hence, the axial viscous force is the main component of the total viscous force.



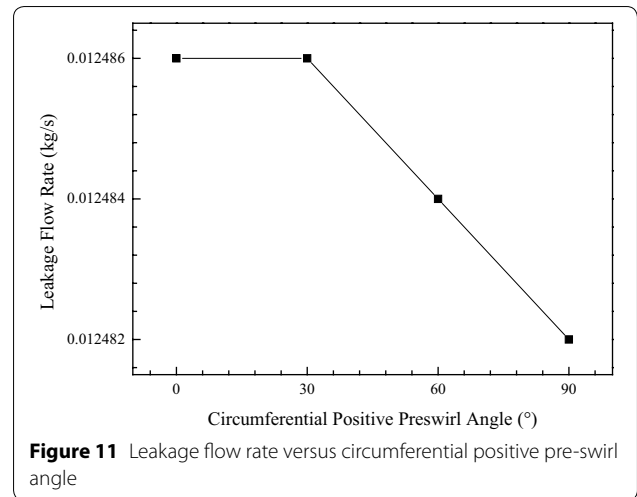
5.4 Effects of the Circumferential Positive Pre-swirl

To investigate the effects of the circumferential positive pre-swirl angle on the fluid-induced force of the RSTLGS, the leakage flow rates, pressure forces, and viscous forces



were computed for four circumferential positive pre-swirl angles at a pre-swirl velocity (100 m/s).

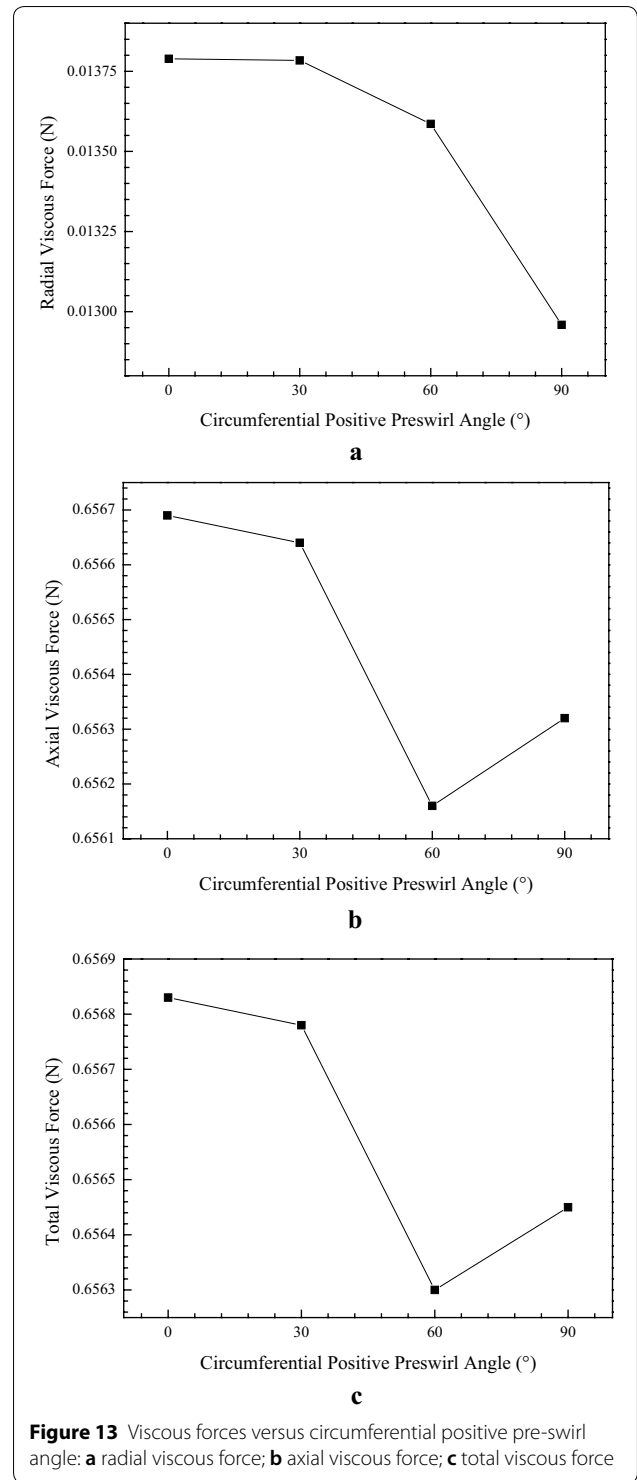
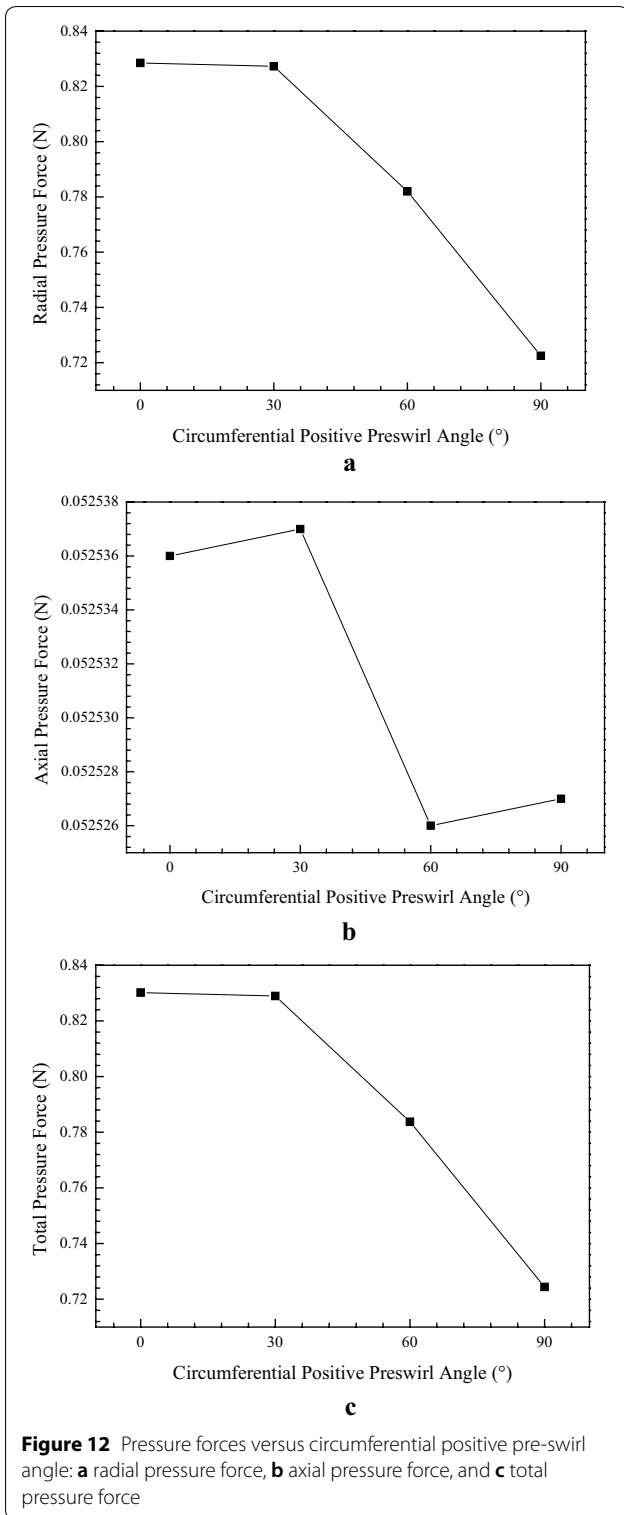
Figure 11 illustrates the dependence of the leakage flow rates for all four circumferential positive pre-swirl angles. With increasing circumferential positive pre-swirl angle,



the leakage flow rate decreases by approximately 0.03% from 0.012486 kg/s at 0° to 0.012482 kg/s at 90°. Therefore, the leakage flow rate decreases with increasing circumferential positive pre-swirl angle.

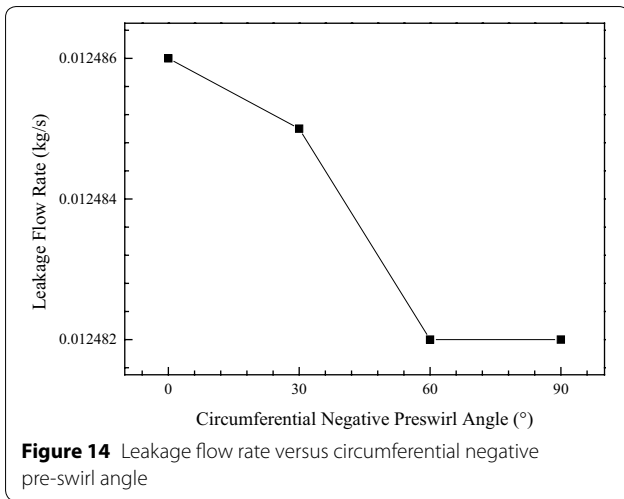
Figure 12 illustrates the dependence of the pressure forces on the rotor surface for all four circumferential positive pre-swirl angles. With increasing circumferential positive pre-swirl angle, the radial pressure force decreases by approximately 12.80% from 0.828514 N at 0° to 0.722497 N at 90°. With increasing circumferential positive pre-swirl angle, the axial pressure force first increases approximately 0.002% from 0.052536 N at 0° to 0.052537 N at 30°, subsequently decreases approximately 0.02% from 0.052537 N at 30° to 0.052526 N at 60°, and then increases approximately 0.002% from 0.052526 N at 60° to 0.052527 N at 90°; a peak at 30° and a valley at 60° appear. With increasing circumferential positive pre-swirl angle, the total pressure force decreases by approximately 12.74% from 0.830178 N at 0° to 0.724404 N at 90°. Therefore, the radial and total pressure forces decrease with increasing circumferential positive pre-swirl angle; the axial pressure force first increases, subsequently decreases, and then increases with increasing circumferential positive pre-swirl angle. The radial pressure force is much larger than the axial pressure force; hence, the radial pressure force is the main component of the total pressure force.

Figure 13 illustrates the dependence of the viscous forces on the rotor surface for all four circumferential positive pre-swirl angles. With increasing circumferential positive pre-swirl angle, the radial viscous force decreases by approximately 6.02% from 0.013789 N at 0° to 0.012959 N at 90°. With increasing circumferential positive pre-swirl angle, the axial viscous force first decreases by approximately 0.08% from 0.656690 N



at 0° to 0.656160 N at 60°, and subsequently increases by approximately 0.02% from 0.656160 N at 60° to 0.656320 N at 90°; a valley at 60° appears. With increasing circumferential positive pre-swirl angle, the total

viscous force first decreases by approximately 0.08% from 0.656835 N at 0° to 0.656301 N at 60°, and subsequently increases by approximately 0.02% from 0.656301 N at 60° to 0.656448 N at 90°; a valley at 60° appears. Therefore,



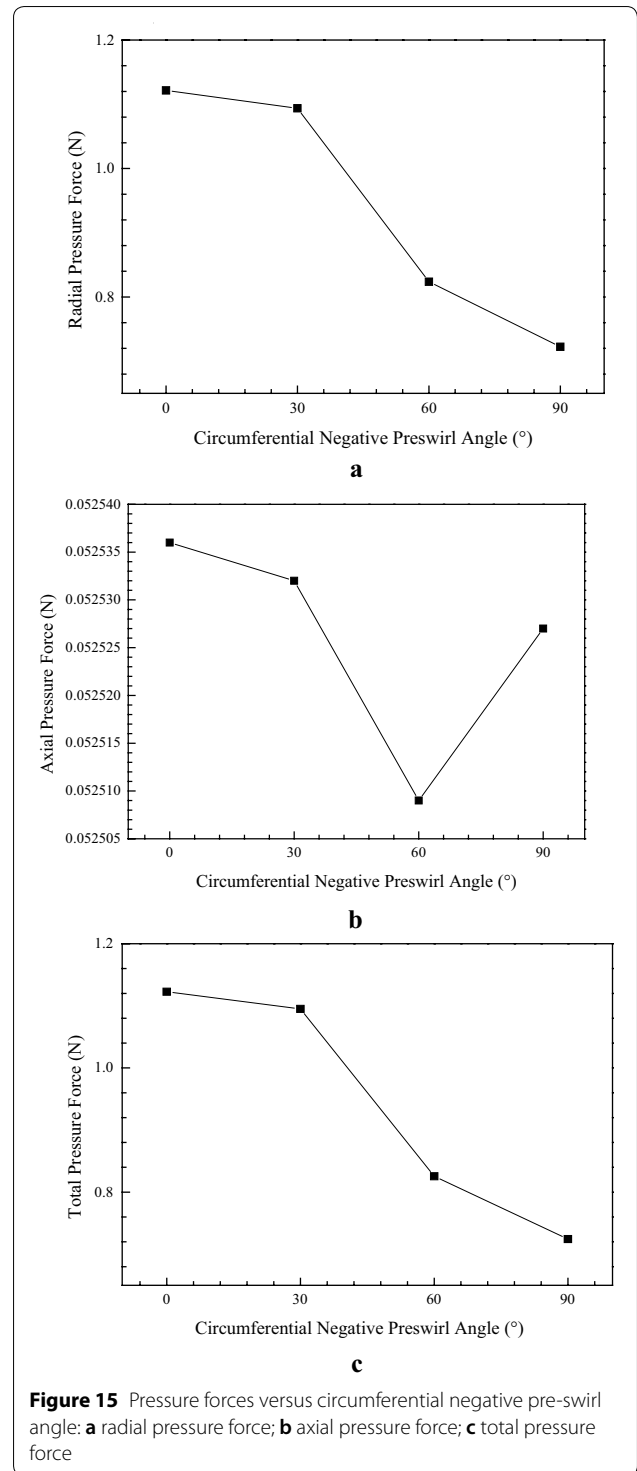
the radial viscous force decreases with increasing circumferential positive pre-swirl angle; the axial and total viscous forces first decrease and subsequently increase with increasing circumferential positive pre-swirl angle; the axial and total viscous forces show minimum values. The radial viscous force is less than the axial viscous force, and hence, the axial viscous force is the main component of the total viscous force.

5.5 Effects of the Circumferential Negative Pre-swirl

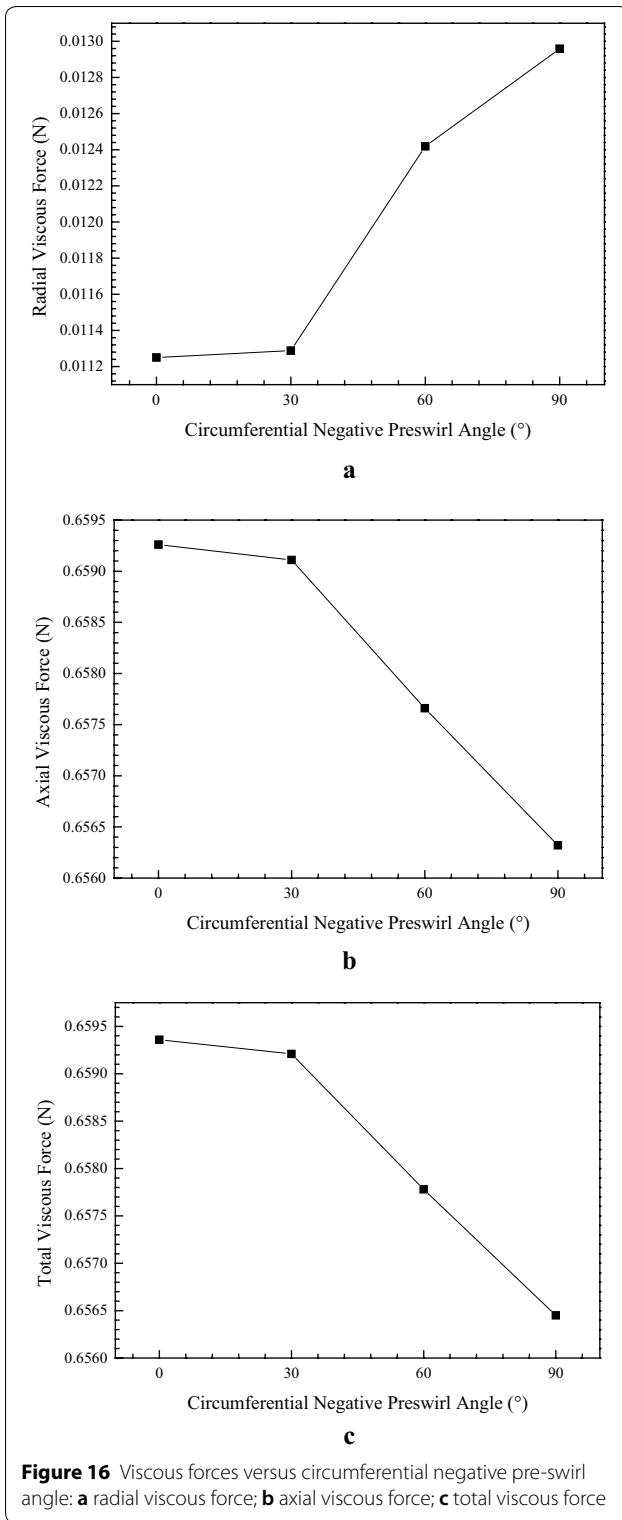
To investigate the effects of the circumferential negative pre-swirl angle on the fluid-induced force of the RSTLGS, the leakage flow rates, pressure forces, and viscous forces were computed for four circumferential negative pre-swirl angles at a pre-swirl velocity (100 m/s).

Figure 14 illustrates the dependence of the leakage flow rates for all four circumferential negative pre-swirl angles. With increasing circumferential negative pre-swirl angle, the leakage flow rate decreases by approximately 0.03% from 0.012486 kg/s at 0° to 0.012482 kg/s at 90°. Therefore, the leakage flow rate decreases with increasing circumferential negative pre-swirl angle.

Figure 15 illustrates the dependence of the pressure forces on the rotor surface for all four circumferential negative pre-swirl angles. With increasing circumferential negative pre-swirl angle, the radial pressure force decreases by approximately 35.58% from 1.121509 N at 0° to 0.722497 N at 90°. With increasing circumferential negative pre-swirl angle, the axial pressure force first decreases by approximately 0.05% from 0.052536 N at 0° to 0.052509 N at 60°, and subsequently increases by approximately 0.03% from 0.052509 N at 60° to 0.052527 N at 90°; a valley at 60° appears. With increasing circumferential negative pre-swirl angle, the total



pressure force decreases by approximately 35.48% from 1.122739 N at 0° to 0.724404 N at 90°. Therefore, the radial and total pressure forces decrease with increasing circumferential negative pre-swirl angle; the axial pressure force first decreases and subsequently increases with



increasing circumferential negative pre-swirl angle; the axial pressure force shows a minimum value. The radial pressure force is much larger than the axial pressure

force, and hence, the radial pressure force is the main component of the total pressure force.

Figure 16 illustrates the dependence of the viscous forces on the rotor surface for all four circumferential negative pre-swirl angles. With increasing circumferential negative pre-swirl angle, the radial viscous force increases by approximately 15.19% from 0.011250 N at 0° to 0.012959 N at 90°; the axial viscous force decreases by approximately 0.45% from 0.659260 N at 0° to 0.656320 N at 90°; the total viscous force decreases by approximately 0.44% from 0.659356 N at 0° to 0.656448 N at 90°. Therefore, the radial viscous force increases with increasing circumferential negative pre-swirl angle; the axial and total viscous forces decrease with increasing circumferential negative pre-swirl angle. The radial viscous force is less than the axial viscous force, and hence, the axial viscous force is the main component of the total viscous force.

5.6 Comparison of the Four Types of Pre-swirls

Four types of pre-swirls, which include the axial pre-swirl, radial pre-swirl, circumferential positive pre-swirl, and circumferential negative pre-swirl in this work, affect the leakage and fluid-induced force of the RSTLGS.

The increasing axial pre-swirl velocity decreases the leakage flow rates, pressure forces, and viscous forces. The results indicate that the velocity magnitude of pre-swirl inhibits the leakage and fluid-induced force, but the change is not evident with increasing axial pre-swirl velocity.

With increasing radial pre-swirl angle, the total pressure force shows the maximum value at 60°, the total viscous force shows the minimum value at 60°, and increasing radial pre-swirl angle decreases the leakage flow rates. The results indicate that the pressure forces and viscous forces show the maximum or minimum value at a specific radial pre-swirl angle.

The increasing circumferential positive pre-swirl angle decreases the leakage flow rates, pressure forces, and viscous forces. The results indicate that the circumferential positive pre-swirl angle promotes the leakage flow rates, pressure forces, and viscous forces.

The increasing circumferential negative pre-swirl angle decreases the leakage flow rates, pressure forces, and viscous forces. The results indicate that the circumferential negative pre-swirl angle promotes the leakage flow rates, pressure forces, and viscous forces.

Table 6 lists the comparison of the maximum change rate of the four types of pre-swirls. The pre-swirl significantly affects the total pressure force, and the circumferential negative pre-swirl has the greatest influence, followed by the circumferential positive pre-swirl. The

Table 6 Maximum change rate of the four types of pre-swirls

Pre-swirl	Maximum change rate (%)		
	Total pressure force	Total viscous force	Leakage flow rate
Axial	3.29	0.04	0.02
Radial	1.42	0.05	0.02
Circumferential positive	12.74	0.08	0.03
Circumferential negative	35.48	0.44	0.03

pre-swirl has some influence on the total viscous force, and the circumferential negative pre-swirl has the greatest influence. The pre-swirl has a negligible impact on the leakage flow rate.

6 Conclusions

- (1) The steady CFD method is proposed based on the three-dimensional model of the RSTLGS and consists of the following parts. The commercial software ANSYS DesignModeler 17.0 is used to establish the three-dimensional computational model. The commercial software ANSYS ICEM CFD 17.0 is used to generate the unstructured mesh for the calculations. The commercial software ANSYS-CFX 17.0 is used to solve the RANS equations. The mesh analysis ensures the accuracy of the steady CFD method.
- (2) To investigate the effects of four types of pre-swirls, computations were performed for six axial pre-swirl velocities, four radial pre-swirl angles, four circumferential positive pre-swirl angles, and four circumferential negative pre-swirl angles using the steady CFD method.
- (3) The axial pre-swirl velocity remarkably inhibits the fluid-induced force, and the circumferential positive pre-swirl angle and circumferential negative pre-swirl angle remarkably promote the fluid-induced force. The effects of the radial pre-swirl angle on the fluid-induced force are complicated, and the pressure forces and viscous forces show the maximum or minimum value at a specific radial pre-swirl angle. The pre-swirl has a negligible impact on the leakage. The four types of pre-swirls affect the leakage, flow field, and fluid-induced force of the RSTLGS in varying degrees.
- (4) The pre-swirl is the influence factor affecting the leakage, flow field, and fluid-induced force of the RSTLGS. The conclusions of this paper will help better understand the fluid-induced force of labyrinth seals by providing helpful suggestions for

engineering practices and a theoretical basis to analyze the fluid–structure interaction of the seal-rotor system in future research.

Authors' Contributions

LH was in charge of the whole trial; QW wrote the manuscript and assisted with sampling and laboratory analyses. Both authors read and approved the final manuscript.

Author Details

¹ Beijing Key Laboratory of Health Monitoring and Self-Recovery for High-End Mechanical Equipment, Beijing University of Chemical Technology, Beijing 100029, China. ² College of Mechanical and Electrical Engineering, Beijing University of Chemical Technology, Beijing 100029, China.

Authors' Information

Qingfeng Wang, born in 1977, is currently a lecturer at *College of Mechanical and Electrical Engineering, Beijing University of Chemical Technology, China*. He received his PhD degree from *Beijing University of Chemical Technology, China*, in 2018. His research interests include turbomachinery seal and CFD.

Lidong He, born in 1963, is currently a professor at *College of Mechanical and Electrical Engineering, Beijing University of Chemical Technology, China*. He received his PhD degree from *Harbin Institute of Technology, China*, in 1999. His research interests include seal fluid-induced vibration, Honeycomb seal, vibration damping technology and active vibration control.

Competing Interests

The authors declare that they have no competing interests.

Funding

Supported by National Basic Research Program of China (973 Program, Grant No. 2012CB026006).

Received: 18 January 2019 Accepted: 29 May 2019

Published online: 20 June 2019

References

- [1] S Claire. *Gas turbines: a handbook of air, land and sea applications*. Oxford, UK: Elsevier, 2015.
- [2] S Subramanian, A S Sekhar, B V S S Prasad. On the choice of initial clearance and prediction of leakage flow rate for a rotating gas turbine seal. *Proceedings of the Institution of Mechanical Engineers, Part C: Journal of Mechanical Engineering Science*, 2016, 230(10): 1586-1601.
- [3] A Rapisarda, A Desando, E Campagnoli, et al. Rounded fin edge and step position effects on discharge coefficient in rotating labyrinth seals. *Journal of Turbomachinery*, 2016, 138(1): 011005.
- [4] R Flitney. *Seals and sealing handbook*. Holland: Elsevier, 2014.
- [5] Z G Li, J Li, Z P Feng. Labyrinth seal rotordynamic characteristics part I: operational conditions effects. *Journal of Propulsion and Power*, 2016, 32(5): 1199-1211.
- [6] Q F Wang, L D He. Effect and sensitivity analysis of the rotational speed on the fluid-induced force characteristics of the straight-through labyrinth gas seal. *High Technology Letters*, 2018, 24(11): 62-74.
- [7] M Schobeiri. *Turbomachinery flow physics and dynamic performance*. Germany: Springer-Verlag, 2005.
- [8] J M Vance. *Machinery vibration and rotordynamics*. USA: Wiley, 2010.
- [9] C Delebarre, V Wagner, J Y Paris, et al. An experimental study of the high speed interaction between a labyrinth seal and an abradable coating in a turbo-engine application. *Wear*, 2014, 316(1-2): 109-118.
- [10] J Alford. Protection of labyrinth seals from flexural vibration. *Journal of Engineering for Power*, 1964, 86: 141-147.
- [11] G Vannini, M Bertoneri, K K Nielsen, et al. Experimental results and computational fluid dynamics simulations of labyrinth and pocket damper

- seals for wet gas compression. *Journal of Engineering for Gas Turbines and Power*, 2015, 138(5): 052501.
- [12] A Muszynska. *Rotordynamics*. USA: CRC Press, 2005.
- [13] A Muszynska, D E Bently. Anti-swirl arrangements prevent rotor/seal instability. *Journal of Vibration, Acoustics, Stress, and Reliability in Design*, 1989, 111(2): 156-162.
- [14] G Vannini, C Mazzali, H Underbakke. Rotordynamic computational and experimental characterization of a convergent honeycomb seal tested with negative preswirl, high pressure with static eccentricity and angular misalignment. *Journal of Engineering for Gas Turbines and Power*, 2016, 139(5): 052502.
- [15] N R Morgan, H G Wood, A Untaroiu. Design of experiments to investigate geometric effects on fluid leakage rate in a balance drum seal. *Journal of Engineering for Gas Turbines and Power*, 2016, 138(7): 072506.
- [16] X Z Kong, G W Liu, Y X Liu, et al. Experimental testing for the influences of rotation and tip clearance on the labyrinth seal in a compressor stator well. *Aerospace Science and Technology*, 2017, 71: 556-567.
- [17] F Cangioli, P Pennacchi, G Vannini, et al. Effect of energy equation in one control-volume bulk-flow model for the prediction of labyrinth seal dynamic coefficients. *Mechanical Systems and Signal Processing*, 2018, 98: 594-612.
- [18] F Cangioli, S Chatterton, P Pennacchia, et al. Thermo-elasto bulk-flow model for labyrinth seals in steam turbines. *Tribology International*, 2018, 119: 359-371.
- [19] N M Wang, Y R Wang, A M Tian. Influence of structure parameters on aeroelastic stability for labyrinth seal based on energy method. *Propulsion and Power Research*, 2018, 7(4): 288-295.
- [20] J J Moore. Three-dimensional CFD rotordynamic analysis of gas Labyrinth seals. *Journal of Vibration and Acoustics*, 2003, 125(4): 427-433.
- [21] T Hirano, Z Guo, R G Kirk. Application of computational fluid dynamics analysis for rotating machinery—part II labyrinth seal analysis. *Journal of Engineering for Gas Turbines and Power*, 2005, 127(4): 820-826.
- [22] A O Pugachev, U Kleinhans, M Gaszner. Prediction of rotordynamic coefficients for short labyrinth gas seals using computational fluid dynamics. *Journal of Engineering for Gas Turbines and Power*, 2012, 134(6): 062501.
- [23] Z G Li, J Li, X Yan, et al. Numerical investigations on the leakage and rotordynamic characteristics of pocket damper seals—part I effects of pressure ratio, rotational speed, and inlet preswirl. *Journal of Engineering for Gas Turbines and Power*, 2014, 137(3): 032503.
- [24] S Subramanian, A S Sekhar, B V S S Prasad. Rotordynamic characteristics of rotating labyrinth gas turbine seal with centrifugal growth. *Tribology International*, 2016, 97: 349-359.
- [25] L N Butymova, V Y Modorskii. Numerical modeling of the labyrinth seal taking into account vibrations of the gas transmittal unit rotor in aeroelastic formulation. *Procedia Engineering*, 2017, 201: 666-676.
- [26] Z G Li, J Li, Z P Feng. Labyrinth seal rotordynamic characteristics part II: geometrical parameter effects. *Journal of Propulsion and Power*, 2016, 32(5): 1281-1291.
- [27] Z G Li, J Li, Z P Feng. Numerical comparisons of rotordynamic characteristics for three types of labyrinth gas seals with inlet preswirl. *Proceedings of the Institution of Mechanical Engineers, Part A: Journal of Power and Energy*, 2016, 230(7): 721-738.
- [28] A Untaroiu, N Morgan, V Hayrapetian, et al. Dynamic response analysis of balance drum labyrinth seal groove geometries optimized for minimum leakage. *Journal of Vibration and Acoustics*, 2017, 139(2): 021014.
- [29] ANSYS. *CFX user document, Version 17.0*. Europe: ANSYS, 2015.

Submit your manuscript to a SpringerOpen[®] journal and benefit from:

- Convenient online submission
- Rigorous peer review
- Open access: articles freely available online
- High visibility within the field
- Retaining the copyright to your article

Submit your next manuscript at ► [springeropen.com](https://www.springeropen.com)
